Peter M. Arronax Consultants, Ltd.
1954 S. Quid Street, Captainee, MO 61057

To: Mr. J. A. Mesmason, Crew Chief
Nautilus Salvage, Inc., 20000 Buena Vista Avenue, Vulcania, Hawaii 96807

From: J. Liu, T. Nerurkar, C. Wang, F. Xia, Test Engineers, Section 12, Team 4

Subject: Active Sonar Pod Shape Proposal with Minimized Drag

Date: April 22, 2014

Dist: Mr. K. Douglass, Testing Lead, Peter M. Arronax Consultants, Ltd.
Dr. J. U. Lesverne, President Emeritus, Nautilus Salvage, Inc.

FOREWORD

To extend your stationary seafloor salvage operations to mobile seafloor scanning via a towed deep-water high-resolution active sonar system, your company plans to use a cubical submersible pod with edge dimensions of 5.0 m that will be towed and powered through a long cable. To assess whether you should proceed with a design concept of adding a shaped nose cone to the upstream side of the pod to reduce drag and thereby, increase towing speeds, you asked as to determine an optimized shape of the sonar pod by testing several different shape designs with design constraints of having a length-divided-by-width aspect ratio of no more than 2.0, a cubical aft shape, and minimized hydrodynamic lift and drag forces. Specifically, you required us to provide you a scaled model of our proposed pod shape, a dimensioned drawing of the model, and the length-scale ratio between this model and the proposed full-scale sonar pod. In addition, you asked us to predict the relationships between: i) the pod towing depth and the tow ship speed, and ii) the maximum tension in the towing cable and the tow ship speed by considering tow ship speeds from 2 to 10 knots and a 5.0 km cable having streamlined symmetrical-foil cross sectional area of 9.5 cm^2, maximum thickness of 2.0 cm, and linear density of 2.98 kg/m. You required us to include 95% uncertainty estimates, explain our assumptions and predictions for the full-scale pod from our scale-model tests, provide shaping principles, and compare the results of the proposed shape to those of a simple rectangular block. Lastly, you asked us to provide results, conclusions and recommendations regarding our proposed pod shape for the towed sonar application. We have completed these tasks. The purpose of this report is to provide our findings, conclusions, recommendations and supporting documentation.

SUMMARY

We refined three shapes from balsa wood rectangular blocks and proposed an optimal shape geometry that satisfied all design constrains with drag and lift coefficients as shown in Fig. 1, p. 2 with detailed dimensioned drawing. The length-scale ratio between the model and the full-scale sonar pod is 100.0 ± 0.2:1. We conducted wind tunnel tests on the wood models and determined drag coefficient and lift coefficient and concluded that the proposed shape has a much lower drag coefficient compared to the rectangular block as shown in Table 1. With 95% uncertainty estimates, we predicted the full-scale pod drag and lift coefficients and justified its validity in terms of 6.19 ± 0.14 % blockage ratio, sting effect correction, and the constant drag and lift coefficient as shown in Fig. 6, and Fig. 7, p. 7. Based on these results, we established both relationships of the pod towing depth and the maximum towing cable tension to the towing ship speed from 2 to 10 knots as shown in Fig. 10, and Fig. 11, p. 9, using force balance analysis on the cable with negligible vertical force. We recommend that you conduct more tests at Reynolds number of 10^7 to justify the constant drag and lift coefficient at high Reynolds number, scale the sonar pod shape accurately for full-scale pod, and check assumptions carefully before using the result.

Table 1: Measured Drag and Lift Coefficients for Rectangular Block and Proposed Shape

Test Object Geometry	Averaged Drag Coefficient (-)	Averaged Lift Coefficient (-)
Rectangular Block	0.983 ± 0.028	0.0048 ± 0.0027
Proposed Shape	0.429 ± 0.017	0.0018 ± 0.0025

PROPOSED SHAPE

To determine the optimal shape of the sonar pod with minimized drag force and lift force, we tested three wooden models with refined shape in the wind tunnel. From the test results, we recommend the symmetric bullet shape geometry with a cubic aft refined from the rectangular block geometry with the drag coefficient of 0.429 ± 0.017, which is less than half of the rectangular block as compared in Table. 6, p. 7. The proposed shape has a length-divided-by-width aspect ratio of 1.9986 ± 0.0011 less than 2.0 as can be determined from the dimensions of top view in Fig. 1(a). This shape satisfies all design constrains. The detailed dimensions of the proposed shape model are shown in Fig. 1 in different views.

Fig. 1: Isometric view of proposed shape model prototype, top view, left side view, and front view of the engineering drawing defined a streamline bullet-like geometry for the proposed shape with rectangular aft and an aspect ratio of 1.9986 ± 0.0011 satisfying all design constrains. Dimensions without labeled error have 1% error tolerance for scaling purpose. All labeled model dimensions have units of millimeter.

(a) Engineering Drawing Top View

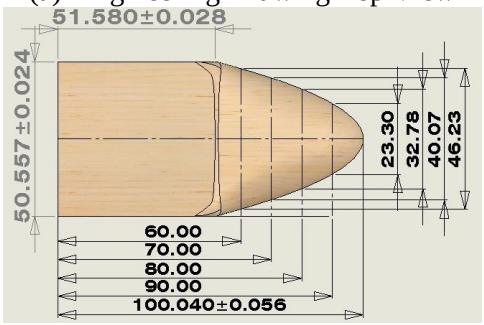

(b) Model Prototype Isometric View

(c) Engineering Drawing Left Side View

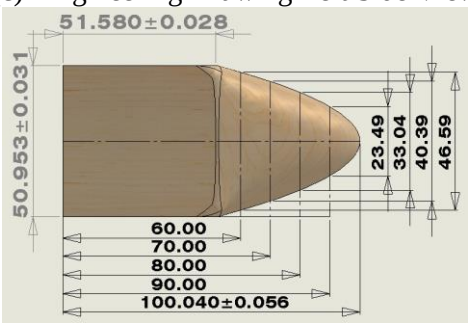

(d) Engineering Drawing Front View

PROCEDURE

To obtain the recommended shape geometry for the sonar pod, we refined three rectangular wood blocks in our inventory to bullet shape of different surface curvature with sandpaper and tested them in the wind tunnel. To determine drag coefficient and lift coefficient of each tested object, we measured dimensions of all test objects, the ambient air condition of the working fluid, and the strain gauge load cell output corresponding to the drag force and lift force. To ensure the quality of the wind tunnel test, we calibrated the strain gauges before each test and measured the effect of the supporting sting alone for data correction.

Proposed Shape Model Fabrication

To refine the front shape of the model from a rectangular block to a bullet, we rubbed one end of the balsa wood block against the sandpaper with both 100 and 150 grit size to remove wood from four of the rectangular vertex. We conducted rubbing process vigorously at first to remove large portion of material and carefully in the end to ensure a good surface finish. To meet the pre specified design constraints, we avoided reducing the length of the original rectangular shape and kept the aft half of the wooden block cubical. After measuring the original geometry of the rectangular blocks and performing wind tunnel tests on the rectangular block, we refined three shapes in total with different surface curvature for comparison.

Model Dimension Measurement

In addition to the detailed dimension of the proposed shape as illustrated from Fig. 1, p. 2, we measured the dimensions and masses of the tested blocks as shown in Table 2 for calculating the blockage ratio and specifying the characteristic length for the Reynolds numbers.

Table 2: Model Dimensions and Mass Measurement.

	Length (mm)	Width (mm)	Height (mm)	Mass (g)
Tested Rectangular Block	101.673 ±0.013	50.557 ±0.024	50.983 ±0.013	26.503 ±0.013
Proposed Shape	100.040 ±0.056	50.557 ±0.024	50.953 ±0.031	15.360 ±0.005
Averaged Rectangular Block	101.328 ±0.043	50.432 ±0.035	50.857 ±0.041	26.328 ±0.037

Pre-test Ambient Pressure and Temperature Measurement

To obtain properties of air at test condition, we measured the ambient pressure and temperature. We used linear interpolation to obtain the density and viscosity of air from tabulated data [1] as shown in Table 3.

Table 3: Ambient Air Properties

Air Temperature(℃)	Air Pressure (10^3Pa)	Air Density (kg/m^3)	Air Viscosity (10^{-5}Ns/m^3)
21.4 ±0.1	98.94 ±0.02	1.1928 ±0.0002	1.8187 ±0.0003

Test Setup and Equipment

To obtain all necessary data for calculating the drag and lift coefficients, we performed tests on the model shapes using a model #122 industrial Air Products wind tunnel with standard three phase alternating current power input. We obtained the wind speed using a Dwyer series 400 air velocity meter with 2% accuracy error. The drag and lift force were measured with a Honeywell model 11 subminiature load cell with accuracy error determined from calibration. A Correx tension gauge with resolution error ±0.05 N was used for drag force measurement calibration and an Ohaus Sto-A-Weigh brass balance weights with negligible error were used for lift force measurement calibration. In addition, a supporting sting with outer average diameter of 6.35 ±0.01mm was used for fixing the test object. We took data from the load cell measurement using LabVIEW 11.0.1 software at a sampling rate of 200 Hz and recorded the lift (mV/V) and drag (mV/V) for a two second period. All test equipment belongs to our testing facility. Detailed schematics of the wind tunnel are depicted in Fig. 2 and Fig. 3.

Fig. 2: Wind tunnel side view with labeled wind direction and strain gauge location illustrates the general setup of the wind tunnel test.

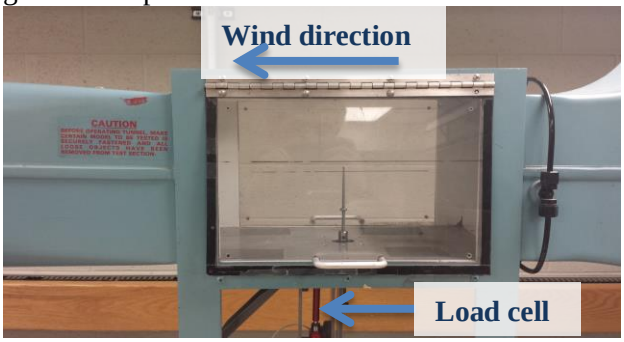

Fig. 3: Wind tunnel inner structure with labeled height and width and the supporting sting location in the middle enables a symmetric load distribution.

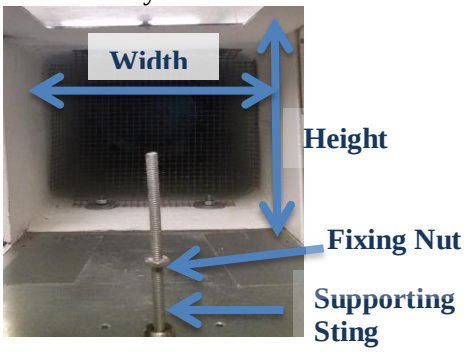

From Fig. 2 and Fig. 3, we noticed that the load cell was located outside of the wind tunnel and therefore does not affect the measurement of drag force and lift force of the wind tunnel. However, the supporting sting will induce some drag force and biased lift force on the measured block for its exposed part in the wind tunnel not covered by the test object. In addition, the wall of the wind tunnel shown in Fig. 3, p. 3 might induce pressure change around the test object due to sudden change of cross section area for fluid

passage. Therefore, correction for the sting and blockage ratio defined by the cross-sectional area of the test object and the wind tunnel inner cross sectional area need to be considered as discussed on p. 5.

Pre-Test Wind Tunnel Dimension and Sting Measurement

To justify the wind tunnel test validity through blockage ratio, we measured the inner width and height of the wind tunnel, length of the extending sting as shown in Fig. 3, p. 3 with result shown in Table 4. The average clearance distances of the block surface to the wind tunnel inner surface for up surface, down surface and side surface are measured as 99.37 ±0.21mm, 52.966 ±0.057mm and 77.035 ±0.016mm.

Table 4: Wind Tunnel, Supporting Sting, and Fixing Nut Dimension Measurement

Object	Height (mm)	Width/Diameter (mm)	Frontal Cross-section Area (mm^2)
Wind Tunnel	203.29 ±0.12	204.62 ±0.02	4159 ±25
Supporting Sting	43.69 ±0.04	4.57 ±0.02	199.7 ± 0.9
Fixture Nut	3.36 ±0.02	10.81 ±0.04	36.3 ± 0.2

Pre-Test Wind Tunnel Calibration

For calibration of the wind tunnel measurement, we double checked the alignment of the strain gauge load cell magnetic component and calibrated the drag force and lift force measurement.

To establish a relationship between the actual drag force and strain gauge load cell reading, we first nulled the sensor reading in LabVIEW with only the supporting sting in place and then applied load from 0 to 2 N with 0.5 N increment on the sting attached to the strain gauge load cell in the horizontal direction with the Correx force meter and recorded the corresponding load cell outputs in LabVIEW. To establish a relationship between the actual lift force and strain gauge load cell reading, we nulled the sensor reading in LabVIEW with a rectangular block fixed onto the supporting sting, placed standard weights from 0 to 50 g with 10 g increment on the block and recorded the corresponding load cell outputs in LabVIEW.

We performed linear curve fits with the known loads from the force meter or the converted force induced by the gravity of the standard weight against their corresponding load cell values. Since gravity force points in the opposite direction of the lift force, we used magnitude of the load cell reading to perform the linear curve fit. The proportional constants from the linear fit as shown in Fig. 4 and Fig. 5 are then used to convert the measured value to the actual drag force or lift force.

Fig. 4: Drag force strain gauge calibration gives a proportional constant value K_D of 4.296 ±0.012 $mVN^{-1}V^{-1}$ that can be used to convert strain gauge measurement to drag force with large correlation coefficient R^2 = 0.9990 indicating good accuracy of the load cell drag measurement.

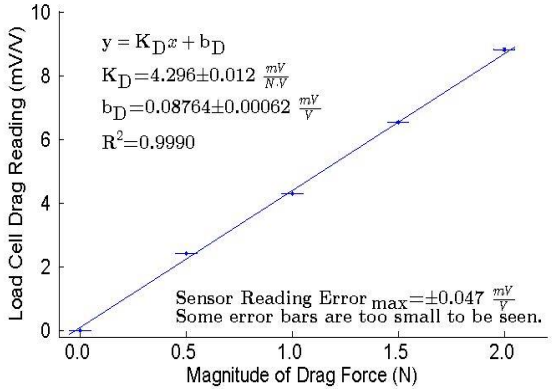

Fig. 5: Lift force strain gauge calibration gives a proportional constant value K_L of 4.001 ±0.010 $mVN^{-1}V^{-1}$ that can be used to convert strain gauge measurement to lift force with large correlation coefficient R^2 = 0.99999992 indicating good accuracy of the load cell lift measurement.

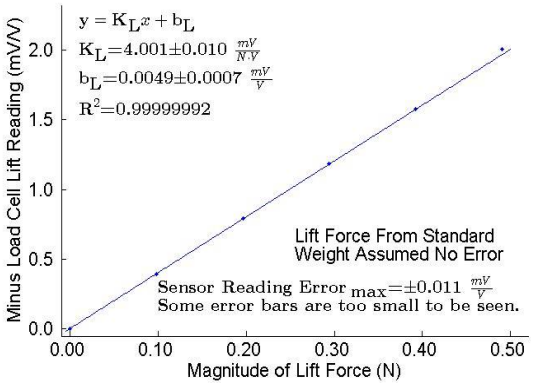

Test Measurement: Varying the Wind Speed
After finishing the measurements and calibration before each experiment, we marked the top side of the test object and fixed the test object firmly onto the supporting sting with the fixing nut. We performed wind tunnel test on one object by increasing the speed of the wind tunnel slowly and taking measurement at an increment of approximately 10 miles per hour (1 mph equals 0.44704 m/s) from 0 to 60 mph. We ran the test again with the object upside down to remove biased lifting effect caused by the sting. The drag and lift forces were recorded in LabVIEW and the velocity was read from the air velocity meter.

FINDINGS
From the wind tunnel load cell measurement of known force, we obtained the calibration curves (Fig. 4 and Fig. 5, p. 4) of the load cell for establishing the actual force and measurement value correspondence. By measuring the inner dimension of the wind tunnel and the dimensions of both the rectangular block and the proposed shape, we obtained the blockage ratio for assessing the validation of the test.

From the drag and lift measurement values at different velocity on both the rectangular block and the proposed shape, we determined the drag coefficient and lift coefficient. We determined the relationship of the drag coefficient and the lift coefficient to the Reynolds number and justified the validity of the model test by considering blockage ratio, sting correction.

From measured the drag and lift coefficients of the model we predicted the drag and lift coefficients of the full-scale pod with justification. We predicted the drag and lift forces of the full-scale pod at different towing speed from 2 knots to 10 knots. Using force balance analysis and the given parameter values, we obtained the relationship of towing depth and the maximum tension on the cable with the towing speed.

Wind Tunnel Model Test Result Validation
To predict the behavior of the full-scale pod operating in sea water, it is easier and much cheaper to test a small scale model in the wind tunnel without having to worry too much about the working fluid leakage or test prototype sealing problem. In addition, through dimensionless parameter similarity, it is not very difficult to predict the full-scale pod performance through test result and reasonable assumption. Therefore the wind tunnel mode test was used to give a good prediction of full-scale pod at low cost. To make the wind tunnel test for the rectangular block and the proposed shape as accurate as possible, several calibration and corrections were used. These considerations contributed to a valid test result.

Sting correction: In calculating the drag coefficient, the drag force on the sting was subtracted from the measured drag force for the test object on the sting. Moreover, the lift coefficient was obtained by half of the difference of the upward and downward placed test object to minimize the effect of the sting.

Blockage ratio: From the measured wind tunnel and test objects dimensions, the blockage ratios for both tests were calculated in Eq. 1:

$$R_b = \frac{A_O}{A_{WT}} = \frac{h_O w_O}{h_{WT} w_{WT}} \quad \text{(Eq. 1)}$$

where R_b = blockage ratio, A_O = test object frontal cross sectional area, A_{WT} = wind tunnel cross sectional area, h_O = test object height, w_O = test object width, h_{WT} = wind tunnel inner height, w_{WT} = wind tunnel inner width. The blockage ratio of the rectangular block test and the proposed shape are 6.20 ± 0.11 % and 6.19 ± 0.14 % respectively. Since the blockage ratios for both test objects are less than 10%, which ensured a negligible effect of the wind tunnel wall on the drag and lift force.

Reynolds Number, Drag Coefficient and Lift Coefficient Determination
To obtain the relationship between the drag and lift coefficients and the Reynolds number, we used the converted drag and lift forces from the calibration curves, and the measured velocity. The formulas for the Reynolds number, the drag and lift coefficients are shown in Eq. 2 to Eq. 4, p. 6, respectively:

$$Re = \frac{\rho u L}{\mu} \quad \text{(Eq. 2)}$$

$$C_D = \frac{F_D}{\frac{1}{2}\rho u^2 A} = \frac{F_{DT} - F_S}{\frac{1}{2}\rho u^2 WH} \quad \text{(Eq. 3)}$$

$$C_L = \frac{F_L}{\frac{1}{2}\rho u^2 A} = \frac{(F_{LU} - F_{LD})/2}{\frac{1}{2}\rho u^2 WH} \quad \text{(Eq. 4)}$$

where Re = Reynolds number, C_D = drag coefficient, C_L = lift coefficient, ρ = density of the fluid, u= relative velocity between the object and the surrounding fluid, L = characteristic length for the object, μ = viscosity of the fluid, A = frontal area of the object, W = width of the rectangular block, H = height of the rectangular block, F_D = drag force, F_{DT} = total drag force for test object and supporting sting, F_S = drag force of the supporting sting without test object, F_L = lift force, F_{LU} = lift force when the test block is upward (prescribed top surface on top), and F_{LD} = lift force when the test block is downward (prescribed top surface on bottom).

In our calculation, the height of the rectangular block was taken as its characteristic length L and the aft height of the proposed shape, which remains unchanged from its original rectangular geometry, was taken as its characteristic length L. The frontal areas of the objects were calculated by the product of the width and height of the original rectangular shape for both the rectangular block and the proposed shape.

Drag force F_D sting correction: The drag force on the test model was determined by using the conversion constant K_D obtained in Fig. 4, p. 4 and subtracting the drag force of the sting without test objects F_S at the same wind speed with values shown in Table 5.

Table 5: Measured Drag and Lift Forces of Supporting Sting for Correction

Wind Speed (m/s)	5.1 ±0.3	9.6 ±0.3	14.2 ±0.4	18.5 ±0.4	23.6 ±0.5	27.9 ±0.6
Drag Force (10^{-3}N)	3.7 ±0.9	14.2 ±2.1	27.5 ±5.4	46.6 ±8.6	68.7 ±9.6	95.2 ±15.4

Lift force F_L sting correction: The lift force on the test model was determined by using the conversion constant K_L obtained from the calibration curve in Fig. 5, p. 4 and half of the difference between the lift force measured at different orientation of the test geometry, specifically, upward F_{LU} and down F_{LD}. Due to the stagnation pressure on the sting being reflected on the test block, simply subtracting the lift force of the sting would yield a biased error of the lift force measurement. Therefore, by taking half of the difference of the tested object placed upward and downward, we eliminated bias error from the sting.

Rectangular Block Drag Coefficient and Lift Coefficient Model-scale Test Result

From the measurement of drag force and lift force at different speed with some conversion and correction, we obtained the relationship of the drag coefficient and lift coefficient to the Reynolds number of the rectangular block and the proposed shape as shown in Fig. 6 and Fig. 7, p. 7, respectively.

From Fig. 6, p. 7, we concluded that the proposed shape has a much smaller drag coefficient than the rectangular block with more than half reduction. From Fig. 7, p. 7, we concluded that the proposed shape has similar lift coefficient as the rectangular block without significant difference. In addition, the value of the lift coefficient fluctuated around 0 at different test speed suggested that the lift effect was very small.

From Fig. 6 and Fig. 7, p. 7, we concluded that the drag and lift coefficients both remained constant regardless of the change of Reynolds number from 10^4 to 10^5 with some small variation. This observation suggested that the drag and lift coefficients do not depend on the Reynolds number. By comparing the values of drag and lift coefficients, we concluded that the lift coefficient of both the rectangular block and the proposed shape were much smaller than their corresponding drag coefficient due to shape symmetry. These observations were later used in predicting the performance of the full-scale pod.

Fig. 6: The drag coefficient of the proposed shape is less than half of that of the rectangular block. The drag coefficients for both geometries remain almost constant regardless of Reynolds number, which is useful for full scale pod prediction.

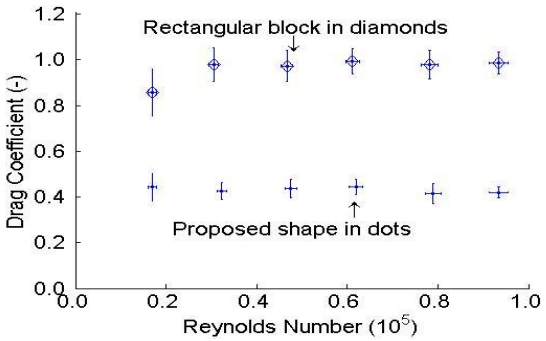

Fig. 7: The lift coefficients of the proposed shape and the rectangular block both fluctuate around 0 with small magnitude regardless of Reynolds number, which is useful for full scale pod performance prediction.

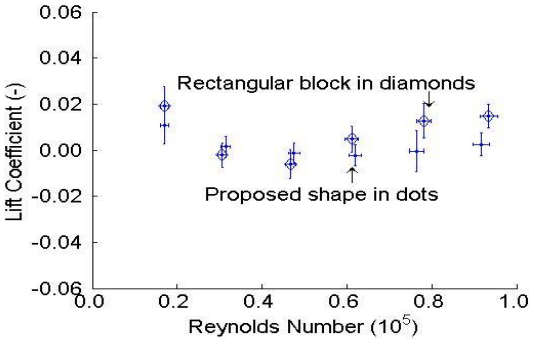

Drag Coefficient and Lift Coefficient Comparison for Rectangular Block and Proposed Shape
In order to make prediction about the full scale model, we computed and compared the averaged value of the drag coefficient and lift coefficient by eliminating obvious measurement outliers at Reynolds number lower than 20000 as shown in Fig. 6 and Fig. 7. The results are shown in Table 6.

Table 6: Drag Coefficient and Lift Coefficient Comparison for Rectangular Block and Proposed Shape

Test Object Geometry	Averaged Drag Coefficient (-)	Averaged Lift Coefficient (-)
Rectangular Block	0.983 ±0.028	0.0048 ±0.0027
Proposed Shape	0.429 ±0.017	0.0018 ±0.0025

From the comparison of the averaged drag and lift coefficients shown in Table 5, we concluded that the proposed shape has a much better performance in terms of its drag coefficient than the rectangular block. For both shapes, the lift coefficients are much smaller than the drag coefficient in magnitude.

Full-scale pod and Tested Model Drag and Lift Coefficients Similarity Justification
To predict the performance of the full-scale pod, several assumptions were needed before we could conclude that the drag and lift coefficient remains the same for the model and the full-scale pod.

Assumptions: During the prediction, we assumed 1) surface roughness, Mach number and Froude Number does not affect drag coefficient and lift coefficient significantly, 2) the drag coefficient and lift coefficient are independent to the Reynolds number could be extended to higher Reynolds number at the magnitude level of 10^7 where the full-scale pod is operating; 3) the operating boundary condition for the wind tunnel test is similar enough to that of the full-scale pod. We justify the assumptions for the drag coefficient below and the case for the lift coefficient can be done similarly.

Dimensionless parameters involved: In general, the drag coefficient is a function of dimensionless parameters as shown in Eq. 4:

$$C_D = f(Re, M, Fr, \frac{\varepsilon}{l}) \quad \text{(Eq. 4)}$$

where C_D = drag coefficient, Re = Reynolds number, M = March number, Fr = Froude number, $\frac{\varepsilon}{l}$ = surface roughness. Since the operating speed of the working fluid in both the wind tunnel test and the sonar pod are both much lower than the sound propagation speed in the medium, Mach number and Froude number effect are negligible. Due to the cubic aft geometry of the tested model, the surface roughness effect can be neglected [2]. This gave the only relevant parameter as the Reynolds number.

Constant drag coefficient extension to higher Reynolds number: From Fig. 6 and Fig. 7 p. 7, we determined that the dimensionless drag and lift coefficients remained constant regardless of the Reynolds number in the region of 10^4 to 10^5. With fixed separation points, this observation can be extended to higher Reynolds number including the magnitude level of 10^7 where the full-scale pod is operating.

Full-scale pod operating environment and tested model condition similarity: The full scale operating in the seawater is surrounded by the seawater far away from solid obstacles such as the sea shore. For the tested model in the wind tunnel, the blockage ratio of 6.19±0.14 %, which is less than 10%, indicated a similar model test condition to the full-scale pod operating environment.

Full-scale pod with Proposed Shape Geometry Drag Force and Lift Force Estimation
To estimate the drag force and lift force of the full-scale pod with the proposed shape geometry, we assumed the drag coefficient and lift coefficient are the same for the proposed shape tested model and proposed shape full-scale pod as justified in the last section. We used Eq. 3 and Eq. 4, p. 6 reversely to solve for the value of the drag force and lift force.

Scaling factor: To estimate the performance of the full-scale pod, we employed a dimension scaling factor of 100.0±0.2:1 for the full-scale pod to the model of the proposed shape.

Fluid properties: The working fluid of the sonar pod being towed is seawater. In the calculation, we used the density value of seawater at 4 ℃ as 1027 kg/m^3 [3].

Relationship of drag force and lift force to towing speed: To estimate the drag force and lift force on the full scale sonar pod with similar geometry as the proposed shape with scaling factor of 100.0±0.2:1 at different towing speed, we used the measured average drag coefficient and lift coefficient, Eq. 3 and Eq. 4, p. 6reversely. To illustrate the relationship of the drag force and lift force to the towing speed, we plotted the drag force versus towing speed and lift force versus towing speed with speed taken with speed taken from 2 knots to 10 knots with 1knot increment as shown in Fig. 8 and Fig. 9.

Fig. 8: Drag force increases proportionally to the square of the towing speed with maximum values equal to 14980±580 N at 5.14 m/s (10 knots) towing speed. Selected ship speed without error and drag force error bars are too small to be seen with maximum value shown.

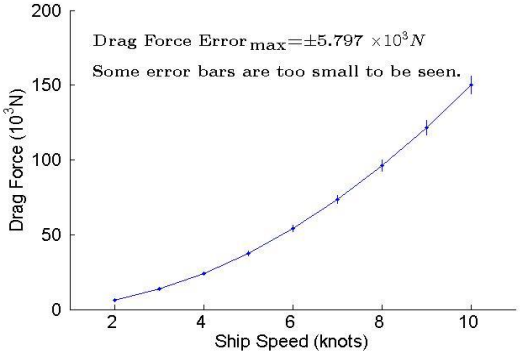

Fig. 9: Lift force increases proportionally to the square of the towing speed with maximum values equal to 640±880 N at 5.14 m/s (10 knots) towing speed. Selected ship speed without error and lift force has large error due to large percentage error at the level of 110% from lift coefficient.

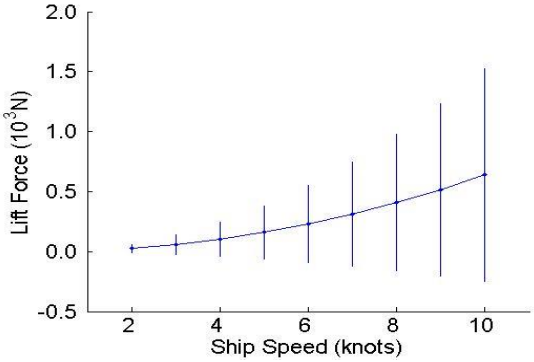

From Fig. 8 and Fig. 9, we concluded that both drag force and lift force are proportional to the square of the ship speed based on the calculation formula and the trend of the curve. The lift force on the magnitude of 640±880 N is much smaller than that of the drag force at 14980±580 N in magnitude at a towing speed 5.14 m/s (10 knots). The major source of error for both drag force and lift force lie within the prediction

and measurement of drag coefficient and lift coefficient of the proposed shape. The large lift force prediction error came from the large percentage error at the level of 110% from lift coefficient.

Relationship of Towing Depth and Maximum Towing Cable Force with Towing Speed

To predict the relationship of the towing depth and maximum towing cable force with the tow ship speed, we established a model and conducted a force balance analysis on the cable with three assumptions: (1) the hydrodynamic loads on the cable are negligible; (2) vertical force on the pod is negligible; and (3) the water is deep enough for the sonar pod. With the maximum thickness of 2.0 cm of the towing cable, the small magnitude of predicted lift force shown in Fig. 9, p. 8 and the active buoyancy control of the sonar pod, and the ocean as operating environment, the three assumptions are satisfied in this case.

From force balance analysis over a differential length of the towing cable, we obtained the governing equation relating the depth and force to the towing speed. With boundary condition considered based on the justified assumptions, we obtained the closed form expression relating the towing depth and maximum force on the cable in Eq. 5 and Eq. 6.

$$T_{max} = \sqrt{g^2(\rho_c - \rho_w A_c)^2 l^2 + {F_D}^2} = \sqrt{g^2(\rho_c - \rho_w A_c)^2 l^2 + (\tfrac{1}{2}\rho_w C_D u^2 A_F)^2} \qquad \text{(Eq. 5)}$$

$$\frac{H}{l} = \frac{F_D}{g(\rho_c - \rho_w A_c) l}\left[1 + \left(\frac{g(\rho_c - \rho_w A_c)}{F_D} l\right)^2\right]^{1/2} = \frac{\frac{1}{2}\rho_w C_D u^2 A_F}{g(\rho_c - \rho_w A_c) l}\left[1 + \left(\frac{g(\rho_c - \rho_w A_c)}{\frac{1}{2}\rho_w C_D u^2 A_F} l\right)^2\right]^{1/2} \qquad \text{(Eq. 6)}$$

where T_{max} = maximum tension on the towing cable, g = the acceleration due to gravity, ρ_c = line density of the cable, ρ_w = density of seawater, A_c = cross sectional area of the cable, l = the length of the cable, F_D = predicted drag force of the sonar pod with proposed shape, A_F = frontal area of the full-scale sonar pod, C_D = predicted drag coefficient of the proposed geometry, H = towing depth and u = towing speed.

With the cable length l taken as 5.0 km, the cross-section area of the cable A_c taken as 9.5 cm^2, the linear density of the cable ρ_c taken as 2.98 kg/m, the acceleration due to gravity g taken as 9.81m/s^2 [4], and the density of seawater ρ_w taken as 1027kg/m^3, we calculated the towing depth and maximum cable tension with the dimension of the proposed shape scaled up to 100 ±0.2 .We plotted the drag force versus towing speed and lift force versus towing speed with speed taken with speed taken from 2 knots to 10 knots with 1knot increment and connected all data points directly as shown in Fig. 10 and Fig. 11.

Fig. 10: Towing depth demonstrated a decreasing trend with the increase of the ship speed. Selected ship speed was assumed to have no error.

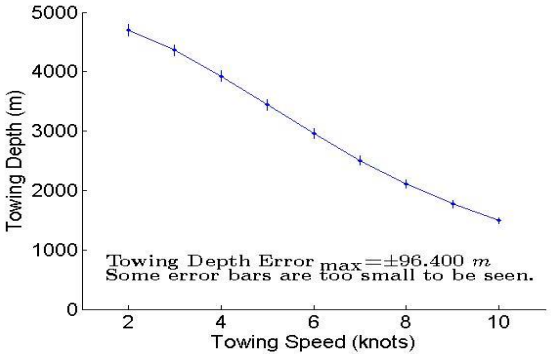

Fig. 11: Maximum cable tension demonstrated an increasing trend with the increase of the ship speed. Selected ship speed was assumed to have no error.

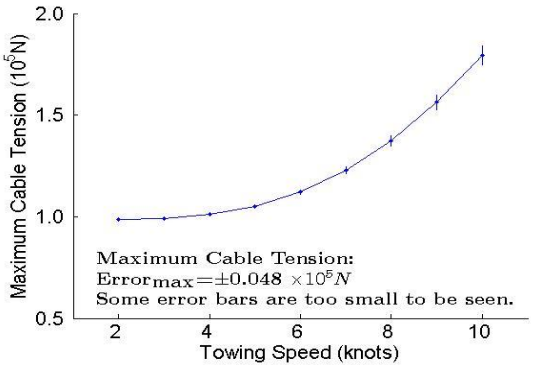

From Fig. 10, we concluded that the towing depth decreases with the increase of the towing speed at an almost constant pace without much change in decreasing speed. From Fig. 11, we concluded that the

maximum cable tension increases with the increase of towing speed and the higher the towing speed, the faster the maximum cable tension increases. These results indicated that the towing speed needs to be carefully controlled if the sonar pod is to stay at a fixed depth when taking measurement. In addition, the towing speed cannot be too large as the increasing magnitude of the maximum cable tension may exceed the maximum allowable tension force of the towing cable.

Uncertainty Analysis in Model Measurement and Full-scale Pod Prediction

During the measurement of the drag and lift coefficients of the wood models, there are to major source of error. The first major source of error is the wind speed measurement due to large resolution error of the air velocity meter. The second major source of error lies in the drag calibration done by using a hand-held force meter from which some implementation error due to human operation might be involved. Moreover, the in perfect alignment of the supporting sting which was assumed to be perfectly perpendicular to the wind velocity direction might result in the increasing drag and lift coefficients errors at larger wind speed.

For the prediction of the full-scale pod performance, the major source of uncertainty came from the drag and lift coefficients of the full scale pod which were assumed to be equal to the measured value of the model from wind test with justification. Although many assumptions used were theoretically justified with care, these assumptions may contribute to the uncertainty of the final results which were not included during the prediction. In addition,, the parameter values used according your requirement without error might add more uncertainties to the calculation results in real world application.

CONCLUSION AND RECOMMENDATIONS

We refined three shapes from balsa wood rectangular blocks and proposed an optimal shape geometry that satisfied all design constrains with drag and lift coefficients as shown in Fig. 1, p. 2 with detailed dimensioned drawing. The length-scale ratio between the model and the full-scale sonar pod is 100.0 ± 0.2:1. We conducted wind tunnel tests on the wood models and determined drag coefficient and lift coefficient and concluded that the proposed shape has a much lower drag coefficient compared to the rectangular block as shown in Table 7. With 95% uncertainty estimates, we predicted the full-scale pod drag and lift coefficients and justified its validity in terms of 6.19 ± 0.14 % blockage ratio, sting effect correction, and the constant drag and lift coefficient as shown in Fig. 6, and Fig. 7, p. 7. Based on these results, we established both relationships of the pod towing depth and the maximum towing cable tension to the towing ship speed from 2 to 10 knots as shown in Fig. 10, and Fig. 11, p. 9, using force balance analysis on the cable with negligible vertical force.

Table 7: Measured Drag and Lift Coefficients for Rectangular Block and Proposed Shape

Test Object Geometry	Averaged Drag Coefficient (-)	Averaged Lift Coefficient (-)
Rectangular Block	0.983 ± 0.028	0.0048 ± 0.0027
Proposed Shape	0.429 ± 0.017	0.0018 ± 0.0025

Based on the limitation of the test measurements and assumptions made during the prediction for drag coefficient and lift coefficient, we have several recommendations to help you understand the result for the proposed shape and get more accurate results. First, since the tested model Reynolds number is at the level of 10^5 due to limited size and maximum wind speed of the wind tunnel, we recommend that you conduct further tests at Reynolds number level of 10^7 to justify the high range Reynolds number independence of drag and lift coefficients. Second, since the scaling factor directly affects the predicted drag force on the towing pod greatly, the sonar pod shape need accurate length-scale ratio of 100 ± 0.2:1 for the full-scale pod for the towing depth and maximum cable tension prediction to be valid. The calculation should be redone for changed length-scale ratio. Lastly, the prediction of the full-scale pod performance only works when the justified assumptions listed in the report are satisfied. Hence, we recommend that you check through each of the assumptions carefully to see if they are satisfied for the specific application before using the results.

REFERENCES

[1] Bergman, T.L., Lavine, A.S., Incropera, F.P., Dewitt, D.P., 2011, *Fundamentals of Heat and Mass Transfer*, John Wiles & Sons, pp. 995, Appendix A.

[2] Munson, B.R., Okiishi, T.H., Huebsch, W.W., Rothmayer, A.P., 2013, *Fundamentals of Fluid Mechanics*, John Wiles & Sons, pp. 520, Chapter 9.

[3] Windows to the Universe, 2008, "Density of Ocean Water", Windows to the Universe website, accessed at http://www.windows2universe.org/earth/Water/density.html on 18 April 2014.

[4] National Institute of Standards and Technology, 2008, "The International System of Units (SI)" NIST website, accessed at http://physics.nist.gov/Pubs/SP330/sp330.pdf on 19 April 2014.